Chemical Science

ROYAL SOCIETY OF CHEMISTRY

EDGE ARTICLE

View Article Online
View Journal | View Issue

Cite this: *Chem. Sci.*, 2025, **16**, 18695

All publication charges for this article have been paid for by the Royal Society of Chemistry

Received 3rd July 2025
Accepted 3rd September 2025

DOI: 10.1039/d5sc04912a

rsc.li/chemical-science

Molecular precursor synthesis of the Rh_2O_3/Fe_2O_3 spherical architecture for enhanced acidic HER activity and durability

Muhammad Zulqarnain,[a] Zheng Wei,[a] Marcell Hollo,[b] Kathleen A. Dunn[b] and Evgeny V. Dikarev *[a]

Efficient hydrogen evolution catalysts that minimize noble metal content while maintaining high activity and durability are critically needed for scalable water electrolysis. Here, we introduce a molecular precursor strategy to synthesize intimately intermixed Rh_2O_3/Fe_2O_3 nanocomposites with precisely controlled 1 : 1 metal ratio. Thermal decomposition of heterobimetallic complex $[Rh(acac)_3Fe(hfac)_2]$ (acac = acetylacetonate, hfac = hexafluoroacetylacetonate) at 300 °C yields 3D spherical Rh_2O_3/Fe_2O_3 architectures without high-temperature sintering. Electrochemical evaluation reveals that Rh_2O_3/Fe_2O_3 requires only 32 mV to reach −10 mA cm^{-2}, dramatically lower than Rh/Rh_2O_3 (140 mV), commercial Rh_2O_3 (260 mV), or α-Fe_2O_3 (210 mV). The Tafel slope investigation of Rh_2O_3/Fe_2O_3 indicates a Volmer–Heyrovsky mechanism with facile proton adsorption and electron transfer, while electrochemical impedance spectroscopy shows its charge-transfer resistance is an order of magnitude lower than that of Rh/Rh_2O_3. Importantly, chronopotentiometry at −10 mA cm^{-2} reveals ultrastable performance with no observable decay over 120 hours, highlighting the exceptional long-term stability of Rh_2O_3/Fe_2O_3. Post-stability microscopy exhibits intact spherical architecture with no signs of sintering or Ostwald ripening. By integrating earth-abundant sesquioxide that promotes oxophilicity, oxygen-vacancy generation, and enhanced conductivity, the title Rh_2O_3/Fe_2O_3 catalyst uses less than half the Rh loading of Rh/Rh_2O_3 while delivering both superior activity and unmatched durability. This work establishes that although both individual Rh_2O_3 and Fe_2O_3 oxides exhibit poor HER activity and stability in acidic media, their intimately intermixed nanocomposite delivers dramatically enhanced performance and long-term stability. The reported mixed-oxide electrocatalyst overcomes the intrinsic limitations of single-phase oxides and provides general guiding principles for designing future high-performance mixed-oxide systems.

Introduction

Global efforts to decarbonize the energy sector have placed hydrogen, particularly when produced by water electrolysis, at the forefront of sustainable fuel strategies.[1,2] Rhodium is renowned for its exceptional catalytic activity in processes ranging from automotive exhaust abatement to fine-chemicals synthesis, has recently emerged as a potent electrocatalyst for both hydrogen evolution and oxidation reactions.[1,3] Building on the promise of rhodium-based materials, several studies have explored diverse Rh nanostructures, such as Rh_2P nanocubes,[4,5] Rh/Si nanoparticles,[6] Rh–MoS_2 hybrids,[7] and various Rh/layered double hydroxide nanosheet morphologies,[8] which exhibit appreciable HER activity but still fall short of platinum benchmarks,[7,9] particularly in alkaline media where reports are sparse and activities are 20–30 times lower than Pt.[1] A noteworthy advance involved Rh–Rh_2O_3 nanostructures on nitrogen-doped carbon, prepared by heat treatment, which leverages a bifunctional mechanism: Rh sites for hydrogen adsorption and Rh_2O_3 clusters for OH^- adsorption, to achieve Pt-comparable performance in both acidic and alkaline media.[1] For reference, commercial Pt/C remains the benchmark HER catalyst, delivering 10 mA cm^{-2} at an overpotential of about 24 mV in acidic electrolyte and about 103 mV in alkaline electrolyte.[1] In contrast, optimized Rh–Rh_2O_3 nanostructures on N-doped carbon can deliver 10 mA cm^{-2} at an overpotential of just 13 mV in acid and 63 mV in base, surpassing Pt/C in both media.[1]

Nevertheless, recent advances in non-rhodium noble-metal systems have achieved even lower overpotentials. For example, platinum anchored on vanadium- and nitrogen-co-doped carbon (Pt@VNC) requires only about 5 mV,[10] Pt–Ni–Rh ternary alloy nanoflowers (Pt_3NiRh NFs) achieve 7 mV,[9] NiCoPt

[a]*Department of Chemistry, University at Albany, SUNY, Albany, NY, 12222, USA. E-mail: edikarev@albany.edu*

[b]*College of Nanoscale Science & Engineering, University at Albany, SUNY, Albany, NY 12203, USA*

alloy nanoparticles reach 8 mV,[11] Ru single atoms together with nitrided Ru nanoparticles implanted on an N-doped graphitic sheet, denoted [Ru(SA) + Ru(NP)@RuNx@GN]/GN,[12] deliver 10 mV in acid and 7 mV in base, Ru single atoms (SAs) and Ru nanoparticles (NPs) embedded in multi-heteroatom-doped carbon (MHC) (RuSAs + RuNPs@MHC) operate at 7 mV,[13] Ru clusters anchored on sodium- and potassium-decorated porous carbon (Ru/Na^+, K^+–PC) achieve 7 mV,[14] and a Ru–Rh single-atom plus nanoparticle hybrid on N-doped graphene (Cu/Rh(SAs) + Cu_2Rh(NPs)/GN) requires about 8 mV.[15] This broader comparison underscores two key insights: (i) well-designed Rh-based nanostructures can rival and even outperform commercial Pt/C under certain conditions, (ii) the emergence of Pt- and Ru-based catalysts achieving near-zero overpotentials establishes extremely stringent performance targets for any new HER catalyst. The key question, therefore, is whether Rh-based catalysts can approach these benchmarks while drastically reducing Rh usage and sustaining performance at practical current densities.

Despite impressive activity, existing Rh-based electrocatalysts depend on high Rh loadings to achieve low overpotentials, a strategy that compounds cost concerns and undermines economic viability.[1] Moreover, chronoamperometric stability tests frequently record potential drifts on the order of 50–100 mV within only a few hours of operation,[8,16] revealing that these materials cannot often maintain their initial performance over extended use, a phenomenon commonly attributed to the Ostwald ripening.[17,18] Consequently, the dual challenge of dramatically lowering noble-metal content while preserving, or even enhancing, long-term catalytic stability remains unresolved.[19,20] Herein, we tackle this challenge by forming composites of Rh_2O_3 with inexpensive, earth-abundant 3d sesquioxides, aiming to deliver high HER performance with lowered Rh consumption and robust durability under realistic operating conditions.

Transition metal sesquioxides, M_2O_3, particularly those of the earth-abundant 3d metals such as Fe and Mn, offer an attractive suite of properties for the hydrogen evolution reaction. Mn and Fe represent non-toxic, widely available elements (iron costs less than \$0.005 per oz *versus* over \$5500 per oz for rhodium)[21,22] and adopt the bixbyite crystal structure type,[23] a defect-tolerant cubic lattice of corner- and edge-sharing [MO_6] octahedra that readily accommodate oxygen vacancies as well as surface hydroxyls.[24,25] This open, vacancy-rich framework not only preserves high surface area when fashioned into nanowires, nanospheres, or other morphologies, but also provides abundant sites for water adsorption and OH^- binding, crucial steps in the Volmer reaction of electrocatalytic water splitting.[26] Particularly, Fe_2O_3 can be readily engineered into nanostructured morphologies such as γ-Fe_2O_3 nanowire arrays, that dramatically expand electrochemical surface area and expose the high-energy edge sites, enabling standalone OER performance (10 mA cm^2 at 1.88 V *vs.* RHE) with short stability ($\approx$9.6 mA cm^{-2} over 3275 s) even without noble metal modulation.[27] While analogous Mn_2O_3 system remains underexplored for HER, prior works on Pt–Y_2O_3 and Pt–Gd_2O_3 composites have shown that M_2O_3 clusters can induce beneficial strain effects and tailor surface interactions, enhancing activity and long-term stability without alloy formation.[28] However, the fusion of Rh_2O_3 bifunctional OH^- adsorption and water-dissociation capabilities with the low cost and robustness of Fe_2O_3 or Mn_2O_3 has yet to be investigated, presenting a clear opportunity to develop highly active, durable, and economically viable HER electrocatalysts.

Typically, sesquioxide materials are prepared by wet chemical routes,[29] co-precipitation,[30] sol–gel,[31] hydrothermal,[23] or solvothermal treatment,[23] often followed by a high-temperature calcination to induce the M^{III} oxide phase.[32,33] In co-precipitation, metal salts (chlorides, nitrates) are mixed and base-titrated, with pH, temperature, and aging time controlling the nucleation rate.[26] This yields particles which size, crystallinity, and polymorphism (for example, α- *vs.* γ-Fe_2O_3, or bixbyite *vs.* MnO_2-derived Mn_2O_3)[25] depend sensitively on the experimental parameters. Sol–gel approach, where metal alkoxides or metal–organic complexes are hydrolyzed in alcohol/water mixtures, enables molecular level mixing but typically requires a post-gelation bake ($\sim$600 °C)[30] to remove organics and crystallize the oxide. Despite their maturity, these conventional approaches suffer from several drawbacks when the goal is a finely tuned sesquioxide electrocatalyst. First, high-temperature calcination required for phase-pure M_2O_3 usually collapses nanoscale porosity, thus reducing electrochemical surface area. Second, controlling the Fe_2O_3 or Mn_2O_3 polymorph (α, γ, ε) and simultaneously achieving small particle size requires a delicate balance of pH, temperature, and ligand environment, conditions that are hard to scale reproducibly.[32]

Molecular precursor approach, where two or more metal centers are bridged within a single molecular complex, offer an attractive alternative to conventional multi-step and high-temperature syntheses for mixed oxides.[34] Upon thermal decomposition, molecular precursors ensure atomically intimate mixing, precise control over the Rh : M ratio, and the formation of uniform nanostructures at the temperatures around 300–400 °C, below those typically required for separate oxides crystallization.[35] Although molecular precursors have proven effective for the low-temperature synthesis of mixed transition-metal oxides, such as Fe–Ni and Bi–M (M = Mn–Zn) heterostructures *via* heteroleptic diketonate complexes,[36,37] their use in crafting finely tuned sesquioxide electrocatalysts remains practically unexplored. This gap leaves an opportunity to synthesize Rh_2O_3/M_2O_3 nanocomposites in a single, scalable step with superior surface area, controlled particle size, and tailored morphology.

Although neither Rh_2O_3 nor M_2O_3 (M = Mn, Fe, Co) alone exhibit significant HER activity,[38,39] studies on Pt–M_2O_3 systems (M = Y, Gd) demonstrate that atomically dispersed oxide clusters can dramatically enhance catalytic kinetics compared to simple physical blends, which tend to segregate and offer limited interfacial synergy.[28] By contrast, coarse mixtures of sesquioxides prepared *via* conventional routes invariably suffer from phase separation and poor charge transfer, underscoring the critical importance of true atomic level mixing to unlock synergistic HER pathways.

In this work, we develop molecular precursors [Rh(acac)$_3$-M(hfac)$_2$] (acac = acetylacetonate, hfac = hexafluoroacetylacetonate), that decompose at 300 °C to yield uniform, three-dimensional spherical Rh_2O_3/M_2O_3 (M = Mn, Fe) nanocomposites with atomic level mixing and exact Rh : M ratios. Decomposition of heterometallic precursors produces intimately blended mixed metal oxides without the high-temperature sintering that normally collapses porosity, thereby preserving a high surface area and tailored pore structure. Using this low-temperature molecular precursor approach, we obtained Rh_2O_3/Fe_2O_3 nanocomposites that, to the best of our knowledge, exhibit the highest HER activity and durability among all reported Rh-based compounds. This exceptional performance highlights the power of finely mixed oxides in achieving superior electrocatalytic performance with reduced noble metal content.

Results and discussion

Design, synthesis and crystal structure of heterometallic Rh^{III}–M^{II} (M = Mn, Fe, Co) precursors

Drawing from the earlier work on mixed-valent iron diketonates,[36] where reaction of Fe(acac)$_3$ with coordinatively unsaturated Fe(hfac)$_2$ yielded discrete Fe^{III}–Fe^{II} heterobimetallic complex, we sought to extend this strategy to Rh–M (M = Mn, Fe, Co) systems with the Rh : M ratio of 1 : 1. To achieve this, we took the previously characterized dinuclear model complexes of the type $M^{III}(acac)_3M^{II}(hfac)_2$ (*e.g.*, $[Fe^{III}(acac)_3Fe^{II}(hfac)_2]$), which are known to undergo clean, low-temperature decomposition to yield phase-pure mixed-transition metal oxides without high-temperature sintering.[36] We have replaced Fe^{III} with Rh^{III} with expectation that the electron-poor Rh^{III} center will be stabilized by the electron-donating acac ligands, while the electron-rich M^{II} (M = Mn, Fe, Co) sites will be chelated by electron-withdrawing hfac ligands thus enabling efficient heterometallic assembly (Fig. 1). This mixed-ligand, mixed-valent approach ensures each precursor combines precisely one Rh^{III} and one M^{II} ion in a single molecular entity, offering volatility, defined stoichiometry, and the intrinsic predisposition for clean, low-temperature conversion into atomically intermixed oxide nanocomposites. By encoding the metal ratio *via* local coordination environment at the molecular level, these heterometallic precursors pave the way for systematically tuning oxide composition, morphology and ultimately electrocatalytic performance.

The Rh-based heterometallic precursors were synthesized *via* a solid-state/gas-phase reaction between Rh(acac)$_3$ and M(hfac)$_2$ (M = Mn, Fe, Co). Equimolar quantities of the two reagents were mixed, loaded into evacuated glass ampules, and sealed under reduced pressure. The ampules were then heated up at moderate temperatures (65–110 °C) in an electric furnace, during which volatile heterobimetallic species sublimed and re-crystallized at the cooler end of the container as plate-shaped crystals. This technique yields highly pure Rh^{III}–M^{II} complexes in 70–85% yields, depending on the transition metal (SI, Table S1).

Single crystal X-ray diffraction analysis of the $[Rh^{III}(acac)_3$-$M^{II}(hfac)_2]$ precursors (M = Mn (**1**), Fe (**2**), Co (**3**)) reveals a robust heterobinuclear architecture in which the trivalent Rh center is tris-chelated by three acac ligands, forming a compact octahedral unit, while the divalent M ion is *cis*-bis-chelated by two hfac ligands. Two additional Rh–O → M bridging

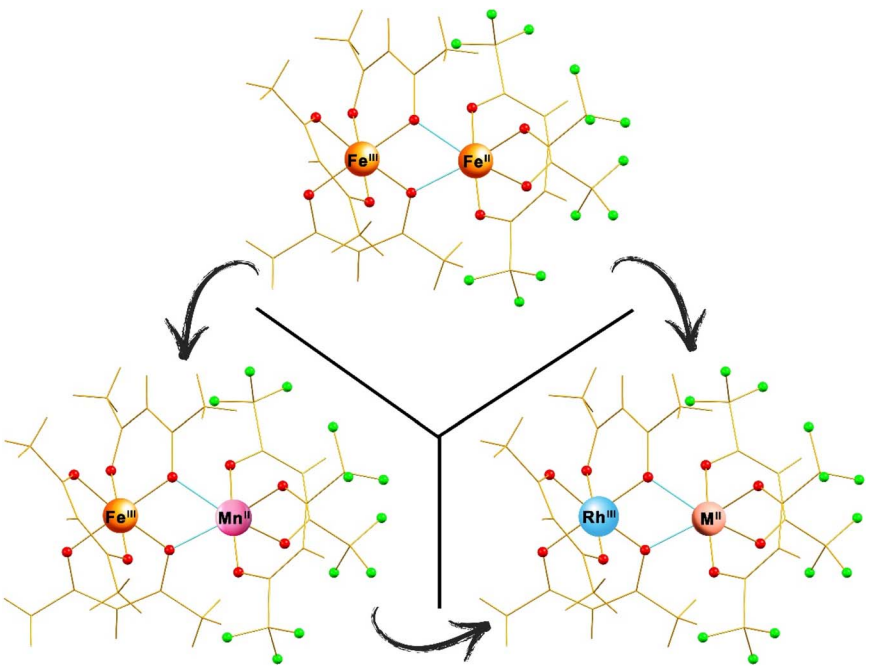

Fig. 1 The design of $[Rh^{III}(acac)_3M^{II}(hfac)_2]$ heterobimetallic precursors based on known homometallic $[Fe^{III}(acac)_3Fe^{II}(hfac)_2]$ and heterometallic $[Fe^{III}(acac)_3Mn^{II}(hfac)_2]$ analogues.

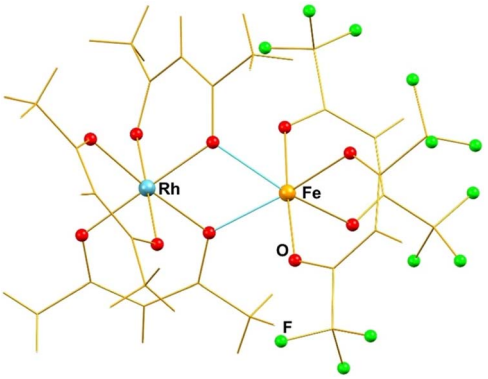

Fig. 2 Solid-state molecular structure of $[Rh(acac)_3Fe(hfac)_2]$ (**2**). The bridging Fe–O bonds are marked as blue. Full views of structures **1–3** with thermal ellipsoids and the full list of bond distances and angles are included in the SI, Fig. S1–S3 and Tables S2–S4, respectively. Complete crystallographic data and refinement parameters are summarized in Tables S5 and S6.

interactions, originating from acac oxygen atoms, complete the M^{II} octahedral coordination, while securing the Rh^{III}–M^{II} linkage within the molecule (Fig. 2). As expected, the electron-donating acac ligands favor coordinating electron-poor Rh^{III} center, whereas the electron-withdrawing hfac ligands selectively bind the electron-richer M^{II} ions, exemplifying the ligand-directed assembly strategy. The Rh–O and M–O bond distances in complexes **1–3** closely match those reported for structurally analogous homo- and heterometallic diketonates, including $[Rh(acac)_3]$, $[Fe(acac)_3Mn(hfac)_2]$,[36] $[Fe(acac)_3Fe(hfac)_2]$,[36] and $[Co(acac)_3Co(hfac)_2]$,[40] thereby supporting the assigned oxidation states of Rh^{III} and M^{II} (Table 1).

Heterobimetallic $[Rh(acac)_3M(hfac)_2]$ complexes (M = Mn (**1**), Fe (**2**), Co (**3**)) exhibit distinct crystalline morphologies appearing as yellow, red, and brown plates, respectively. All three precursors display moderate volatility and can be quantitatively resublimed at the temperatures of 85 (**1**), 65 (**2**), and 110 °C (**3**). Thermal decomposition starts at 140 °C, evidenced by precursor color change to black, indicating sufficient thermal stability. Solubility tests revealed that all three complexes are readily soluble in both non-coordinating (dichloromethane, hexanes) and coordinating (acetone, THF, DMSO) solvents. Notably, these Rh-based precursors demonstrate low air- and moisture sensitivity, a significant advantage over their homometallic $M(hfac)_2$ counterparts, which are known to be highly sensitive to hydrolysis and oxidation. This enhanced stability facilitates straightforward handling, purification, and characterization of precursors outside of a glovebox environment.

The bulk powders for decomposition studies were prepared by grinding the crystalline precursors **1–3** obtained from the solid-state reactions. Phase purity of each material was verified by powder X-ray diffraction: The experimental patterns show excellent agreement with the theoretical ones calculated from the single-crystal X-ray data, as confirmed by the Le Bail fit (Fig. S4–S6 and Tables S7–S9). Additionally, bulk elemental analysis by ICP-OES on precursor **2** yielded an Rh : Fe atomic ratio of 1.03 : 0.97, in excellent agreement with the targeted 1 : 1 stoichiometry. To assess whether the Rh^{III}–M^{II} (M = Mn, Fe, Co) assemblies remain intact in the gas phase, a positive-mode DART (Direct Analysis in Real Time) mass-spectra were acquired (Fig. S7–S9), revealing characteristic heterometallic fragment ions such as $[Rh(acac)_2M(hfac)_2]^+$ ($[M\text{-}acac]^+$) and $[Rh(acac)_3M(hfac)]^+$ ($[M\text{-}hfac]^+$). The experimental isotope distributions of these ions match theoretical patterns, thereby confirming retention of the heterometallic assemblies in the gas phase. Detailed assignments of both homo- and heterometallic ions are provided in Tables S10–S12. The spectra also confirm the Rh(III) and M(II) oxidation states assignment in **1–3** through analysis of the homometallic fragment peaks. Collectively, these data substantiate that all three heterometallic precursors maintain their molecular integrity and metal oxidation states (Rh^{III} and M^{II}) in the gas phase.

Thermal decomposition and morphological analysis of the residues

For the thermogravimetric analysis (TGA) of precursor **2** $[Rh(acac)_3Fe(hfac)_2]$, the sample was heated from 30 °C to 500 °C at the rate of 1 °C min^{-1} (Fig. S10a). An initial mass loss of *ca.* 4% beginning near 85 °C corresponds to the partial volatilization of heterometallic precursor. A more pronounced weight reduction of *ca.* 80% occurs between 200 and 260 °C, attributable to concerted decomposition of the diketonate ligands and release of organic fragments (CO, CO_2, and hydrocarbon moieties). Above 300 °C, the TG trace enters a plateau that extends to 500 °C, indicating complete ligand removal and

Table 1 Comparison of the averaged M–O bond distances in heterometallic precursors **1–3** with those in the corresponding $[Rh^{III}(acac)_3]$ and $[M^{II}(hfac)_2]$ units[a]

Complex	[Ref.]	Rh^{III}–O (Å)	M^{II}–O_c (Å)	M^{II}–O_b[a] (Å)
$[Rh(acac)_3Mn(hfac)_2]$ (**1**)	This work	2.0117(5)	2.1582(5)	2.2795(4)
$[Rh(acac)_3Fe(hfac)_2]$ (**2**)	This work	1.9997(15)	2.0632(16)	2.2350(15)
$[Rh(acac)_3Co(hfac)_2]$ (**3**)	This work	2.0007(14)	2.0455(14)	2.1944(14)
$[Rh^{III}(acac)_3]$	This work	2.0064(9)		
$[Fe(acac)_3Mn^{II}(hfac)_2]$	34		2.1258(17)	2.2033(17)
$[Fe(acac)_3Fe^{II}(hfac)_2]$	34		2.0730(2)	2.1825(2)
$[Fe(acac)_3Co^{II}(hfac)_2]$	40		2.0422(2)	2.1580(2)

[a] O_c: chelating oxygen; O_b: bridging oxygen.

formation of the oxide residue. The isotherm at 300 °C (Fig. S10b) shows a cumulative mass loss of *ca.* 81% over three hours, after which the sample mass remains essentially constant, confirming that ligand decomposition is effectively complete under these conditions. These results establish 300 °C as a suitable thermal treatment temperature for converting the molecular precursor into its oxide form without further weight change, providing a clear basis for subsequent X-ray powder diffraction analysis of the decomposition products.

As the Rh/Rh_2O_3 system is extensively studied for acidic media electrocatalysis,[1,41,42] we first reproduced it by thermal decomposition of [Rh(acac)$_3$] at 400 °C in air. The Le Bail fit of the X-ray powder diffraction pattern (Fig. 3a; see also SI Fig. S11 and Table S13) confirms the presence of metallic Rh and Rh_2O_3 in the residue. Under identical conditions, decomposition of the heterobimetallic precursors **1–3** generates three distinct, mixed oxide composites (Fig. 3b–d, see also SI Fig. S12–S14 and Tables S14–S16). Heating [Rh(acac)$_3$Mn(hfac)$_2$] (**1**) at 300 °C yields exclusively the Rh_2O_3/Mn_2O_3 composite (Table S14), while [Rh(acac)$_3$Fe(hfac)$_2$] (**2**) cleanly decomposes to Rh_2O_3/Fe_2O_3 mixture (Table S15). In contrast, decomposition of the Co-containing precursor **3** produced Rh_2O_3/Co_3O_4 rather than sesquioxide (Fig. 3d), reflecting the stability of Co_3O_4 under these conditions. In all cases, the experimental and calculated diffraction patterns agree closely, underscoring the efficiency of our molecular precursor strategy in delivering intimately blended, multi-oxide nanocomposites without secondary phases or residual organic byproducts. Unlike [Rh(acac)$_3$], whose decomposition yields metallic Rh, the pyrolysis of heterobimetallic molecular precursors **1–3** shows no evidence of metallic Rh presence, underscoring their unique capability to generate oxide-only residues.

Field-emission scanning electron microscopy (FESEM) of the Rh_2O_3/Fe_2O_3 product obtained by decomposition of precursor **2** at 300 °C (Fig. 4(a and b)) reveals the formation of three-dimensional (3D) spherical architectures whose diameter spans roughly from 50 nm to 1.5 μm. These spheres are themselves constructed from primary crystallites on the order of 20 nm, bearing a high surface area. When the decomposition temperature is raised to 400 °C (Fig. 4c), these spheres begin to coalesce, primary particles fuse at their interfaces, producing larger agglomerates with less distinct boundaries. EDS analysis (Fig. S15) confirms the presence of both Rh and Fe, yielding an average Rh : Fe atomic ratio of 1.18 : 1 in the probed region, while elemental mappings (Fig. 4d) indicate an isotropic distribution of Rh and Fe across the sample, as expected from our molecular precursor approach. We note that, without the use of certified standards, EDS provides only semi-quantitative results, and the observed deviation from the nominal 1 : 1 ratio is within the typical accuracy range (≈2–5%) of the technique.

Electrocatalytic performance

Electrocatalytic performance of all synthesized materials was evaluated in 0.5 M H_2SO_4 without *iR* correction using a standard three-electrode cell. The working electrode was a glassy carbon electrode (GCE), modified with the catalyst. To prepare the electrode, 10 mg of catalyst powder was ultrasonically dispersed in 80 μL isopropanol and 20 μL of 5 wt% Nafion solution to form a homogeneous ink, from which 5 μL was drop-cast onto the GCE and air-dried, yielding a catalyst loading of 2.54 mg cm^{-2}. A platinum wire served as the counter electrode, and an Ag/AgCl (saturated KCl) electrode was used as the reference, with all

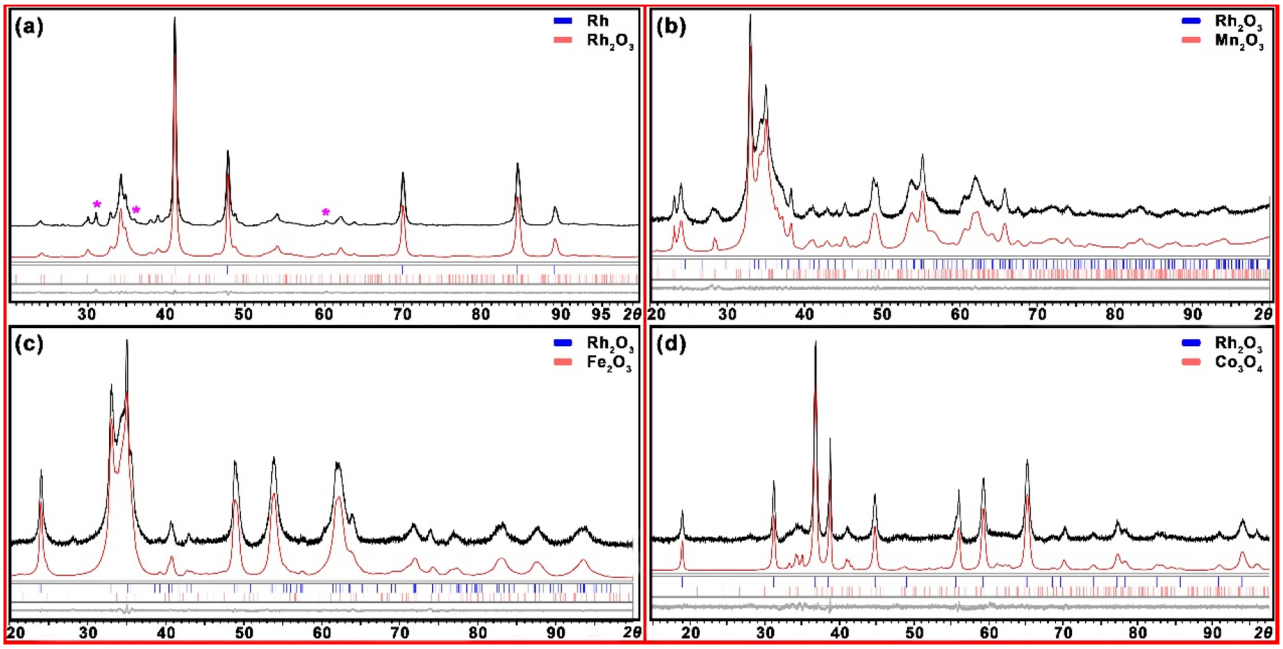

Fig. 3 Powder X-ray diffraction patterns of the residues obtained by thermal decomposition of [Rh(acac)$_3$] (a) and molecular precursors **1–3** (b–d, respectively) with the Le-Bail fit. Black and red curves represent experimental and calculated patterns, respectively. Gray is the difference curve with theoretical peak positions shown as blue and red bars at the bottom. Impurity peaks are marked with asterisk.

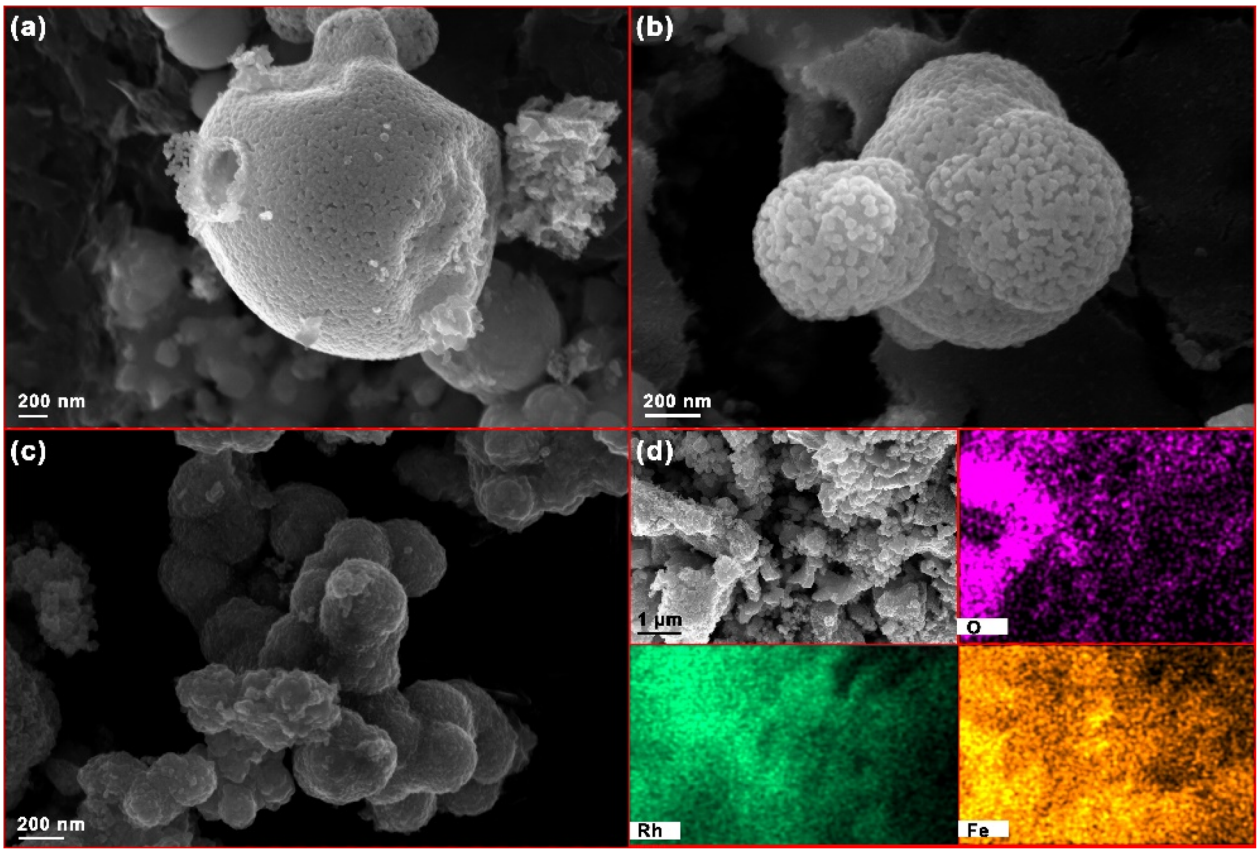

Fig. 4 (a and b) FESEM images of 3D spherical Rh_2O_3/Fe_2O_3 structures obtained by decomposition of molecular precursor $[Rh(acac)_3Fe(hfac)_2]$ (**2**) at 300 °C; (c) FESEM image of the Rh_2O_3/Fe_2O_3 sample obtained at 400 °C showing partial agglomeration of spherical structures; (d) EDS elemental mapping of Rh_2O_3/Fe_2O_3 material synthesized at 300 °C.

potentials converted to the reversible hydrogen electrode (RHE) scale.

Fig. 5a displays LSV curves recorded for commercial Rh_2O_3, commercial α-Fe_2O_3, synthesized Rh/Rh_2O_3, and the three mixed-metal oxide composites (Rh_2O_3/Mn_2O_3, Rh_2O_3/Fe_2O_3, and Rh_2O_3/Co_3O_4). Among those, Rh_2O_3/Fe_2O_3 exhibits the lowest overpotential to reach the current density of −10 mA cm^{-2} (32 mV), markedly outperforming both commercial Rh_2O_3 and α-Fe_2O_3, and even the mixed Rh/Rh_2O_3 reference (76 mV).

It is worth noting that at −10 mA cm^{-2}, Rh_2O_3/Mn_2O_3 requires only 80 mV, nearly matching the overpotential of Rh/Rh_2O_3, whereas Rh_2O_3/Co_3O_4 requires 156 mV, a clear drop in performance. In other words, although Rh_2O_3/Mn_2O_3 and Rh/Rh_2O_3 both benefit from the favorable properties of sesquioxide (M_2O_3) supports, Rh_2O_3/Co_3O_4 fails to deliver similar activity. Co_3O_4 spinel structure inherently suffers from poor electronic conductivity and sluggish redox kinetics,[43] which together raise the overpotential needed for adsorption/desorption steps.[44] By contrast, M_2O_3-type supports (*e.g.* Mn_2O_3, Fe_2O_3, In_2O_3, V_2O_3) are known to readily form oxygen vacancy-rich lattices and offer better oxophilicity,[45–47] both of which stabilize H* intermediates and accelerate charge transfer.

These findings highlight the critical role of sesquioxide support in modulating the interfacial electronic environment and reaction kinetics and demonstrate that integrating Rh_2O_3 with electronically and morphologically compatible Fe_2O_3 offers a powerful strategy to achieve highly efficient HER electrocatalyst. To assess the contribution of ohmic losses, we applied 90% *iR* compensation to the LSVs in 0.5 M H_2SO_4. After correction, η^{10} decreased from 32 to 27 mV and the Tafel slope improved from 84 to 70 mV dec^{-1} (Fig. S16), indicating that a modest fraction of the apparent overpotential arises from solution/contact resistance and that the corrected values more accurately represent the intrinsic HER kinetics of Rh_2O_3/Fe_2O_3. We also compared HER performance for Rh_2O_3/Fe_2O_3 obtained by decomposition of molecular precursor **2** at 300, 400, and 500 °C and found that the activity steadily declines as the decomposition temperature increases (Fig. S17). This degradation parallels our FESEM results: *i.e.*, the higher preparation temperatures cause primary particles to fuse and sinter, reducing accessible surface area. These observations highlight that keeping the synthesis temperature low is essential to preserve nanoscale porosity and maximize active sites for efficient electrocatalytic performance.

In acidic media, the HER mechanism proceeds *via* a Volmer step ($H_3O^+ + e^- \rightarrow H_{ads} + H_2O$; theoretical Tafel slope ≈ 120 mV dec^{-1}) followed either by a Heyrovsky step ($H_{ads} + H_3O^+ + e^- \rightarrow H_2 + H_2O$; ≈ 40 mV dec^{-1}) or a Tafel recombination step ($2H_{ads} \rightarrow H_2$; ≈ 30 mV dec^{-1}).[48] Our measured Tafel slopes reflect how effectively each catalyst facilitates these elementary steps.

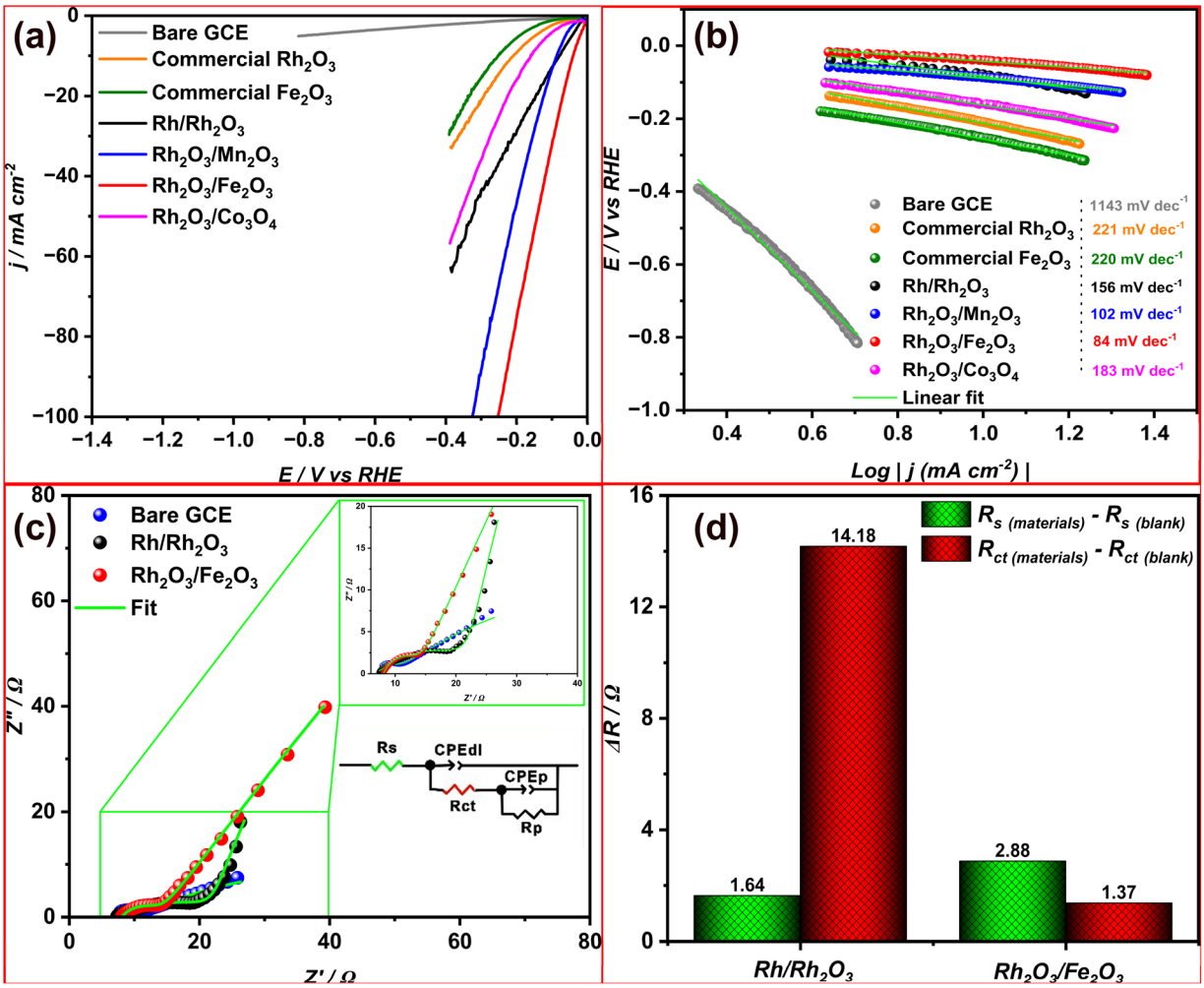

Fig. 5 (a) LSV curves recorded at a scan rate of 100 mV s^{-1} for commercial Rh_2O_3, commercial α-Fe_2O_3, and synthesized Rh/Rh_2O_3, Rh_2O_3/Mn_2O_3, Rh_2O_3/Fe_2O_3, and Rh_2O_3/Co_3O_4 in 0.5 M H_2SO_4 (without *iR* compensation); (b) corresponding Tafel plots derived from the LSV data; (c) Nyquist plots for Rh/Rh_2O_3, Rh_2O_3/Fe_2O_3, and bare GCE, with insets showing magnified semicircle regions and the equivalent circuit used for fitting; (d) comparative plot of charge transfer resistance (ΔR_{ct}) values extracted from EIS data for Rh/Rh_2O_3 and Rh_2O_3/Fe_2O_3 relative to bare GCE.

Commercial Rh_2O_3 and α-Fe_2O_3 exhibit large slopes (~220 mV dec^{-1}), indicating that even the Volmer reaction is rate-limiting. The Rh/Rh_2O_3 mixture improves this to 156 mV dec^{-1}, suggesting partial acceleration of proton discharge. Notably, Rh_2O_3/Mn_2O_3 (102 mV dec^{-1}) and Rh_2O_3/Fe_2O_3 (84 mV dec^{-1}) approach the Volmer–Heyrovsky regime, implying that proton adsorption and subsequent desorption steps both proceed relatively rapidly. These results further demonstrate that M_2O_3 supports significantly lower energy barrier for H_3O^+ reduction relative to homometallic oxides.

Electrochemical impedance spectroscopy (EIS) was performed to quantify the interfacial charge-transfer resistance (R_{ct}) relative to the bare glassy carbon electrode (GCE). In the Nyquist plots (Fig. 5c), the diameter of the high-frequency semicircle reflects the R_{ct} contribution of each catalyst layer superimposed on the intrinsic resistance of the GCE. By fitting these spectra to the equivalent circuit shown in the inset, we extracted the ΔR_{ct} values, defined as R_{ct}(material) − R_{ct}(blank GCE), for each electrode. As plotted in Fig. 5d, Rh/Rh_2O_3 exhibits a ΔR_{ct} of 14.18 Ω, whereas Rh_2O_3/Fe_2O_3 shows a dramatically lower ΔR_{ct} value of 1.37 Ω. This ten-fold reduction in charge-transfer resistance for Rh_2O_3/Fe_2O_3 under identical acidic conditions confirms that the Fe_2O_3 support not only enhances electrical conductivity but also improves the wettability and catalyst–electrolyte interface properties, thereby facilitating faster proton–electron transfer during HER.

To quantitatively compare Rh utilization, we computed Rh mass activity ($j_{mass} = I/m_{Rh}$) and dollar-activity ($I/(m_{Rh} \times$ Rh price)) at a fixed potential of −0.20 V *vs.* RHE by using a previously established normalization procedure.[49] As shown in Fig. S18, Rh_2O_3/Fe_2O_3 delivers approximately 5.71× higher Rh mass activity than Rh/Rh_2O_3. The advantage is amplified in the dollar-activity metric because the 1 : 1 Rh : Fe composition halves the Rh content: Rh_2O_3/Fe_2O_3 achieves approximately 2.56× over Rh/Rh_2O_3 and approximately 54.19× over commercial Rh_2O_3. Together, these analyses show that the mixed-oxide

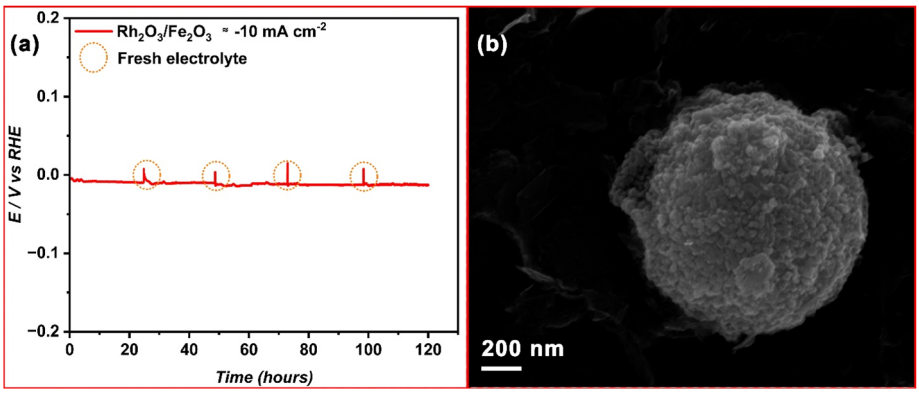

Fig. 6 (a) Chronopotentiometry response of Rh_2O_3/Fe_2O_3 synthesized at 300 °C, recorded for 120 hours at the constant current density of ≈−10 mA cm^{-2} in 0.5 M H_2SO_4; (b) FESEM image of the catalyst after the stability test.

architecture not only lowers overpotential but also delivers much higher current per unit Rh-and per dollar of Rh-highlighting a clear pathway toward cost-efficient HER catalysts.

Comparison of CV scans in the non-faradaic region for Rh/Rh_2O_3 and Rh_2O_3/Fe_2O_3 at sweep rates of 20–120 mV s^{-1} are shown in the Fig. S19. In both cases, the capacitive current scales linearly with scan rate, allowing extraction of the double-layer capacitance (C_{dl}) and electrochemical surface area (ECSA) estimation. The resulting ECSA values indicate that the mixed-metal oxides possess a larger ECSA which is consistent with its superior HER performance. To decouple morphology from intrinsic kinetics, we further normalized the LSVs by ECSA; the resulting curves are shown in Fig. S19. ECSA-normalization collapses geometric effects and enables a like-for-like comparison of interfacial activity per active area.[50] Even on this basis, Rh_2O_3/Fe_2O_3 outperform Rh/Rh_2O_3 across the probed potential window, indicating faster intrinsic HER kinetics rather than a surface-area artefact (Fig. S20). Taken together with the mass-activity analysis, these data show that the mixed-oxide interface delivers genuine catalytic enhancement beyond simple surface exposure.

Chronopotentiometry at ≈−10 mA cm^{-2} (Fig. 6a) demonstrates that Rh_2O_3/Fe_2O_3 prepared at 300 °C maintains a nearly constant potential for the full 120 hours in 0.5 M H_2SO_4. This stability far exceeds previously reported Rh-based electrocatalysts under similar operational conditions, which typically drift by 50–100 mV within only a few hours.[1,8] To the best of our knowledge, Rh_2O_3/Fe_2O_3 demonstrates among the most promising performance and stability reported for Rh-containing HER electrocatalysts under acidic conditions. Notably, this composite outperforms both of its constituents, phase-pure Rh_2O_3 and α-Fe_2O_3, demonstrating the decisive advantage of intimately mixed oxides over the individual components. These findings highlight the critical role of sesquioxide support in modulating the interfacial electronic environment and reaction kinetics and demonstrate that integrating Rh_2O_3 with electronically and morphologically compatible Fe_2O_3 phase offers a powerful strategy to achieve highly efficient HER electrocatalyst.

The post-stability FESEM image (Fig. 6b) confirms that the ~20 nm primary crystallites remain discrete and well-distributed after 120 hours, with no signs of sintering or Ostwald ripening.[18] To directly probe possible metal loss, we analyzedthe electrolyte by ICP-OES before and after the 120 h chronopotentiometry: Rh was below the instrument detection limit at all time points, while Fe showed only trace levels (0.52 mg L^{-1}) after 120 h. Consistently, post-stability EDS elemental mapping (Fig. S21) shows a retained homogeneous Rh–Fe distribution, supporting negligible leaching under our testing conditions. In conventional Rh catalysts, loss of activity is frequently driven by Ostwald ripening,[17] whereby undersized Rh clusters dissolve and redeposit onto larger particles, leading to rapid particle growth and performance decay. In contrast, the intimate atomic-level intermixing of Rh_2O_3 and Fe_2O_3 appears to suppress this mechanism: the Fe_2O_3 matrix, with its high oxygen-vacancy lability, anchors Rh_2O_3 domains, providing lattice-oxygen-mediated "trap" sites that inhibit Rh atom migration and prevent both Rh dissolution and coalescence. Additionally, the preserved mesoporous architecture and uniform Rh–Fe distribution ensure uninterrupted charge-transfer pathways and efficient mass transport, collectively accounting for the exceptional long-term durability of Rh_2O_3/Fe_2O_3. Additionally, Table S17 benchmarks our Rh_2O_3/Fe_2O_3 against Rh containing HER catalysts only. As noted therein, several prior systems-for example, Rh–Cu hybrids and Pt_3NiRh nanoflowers-achieve lower overpotentials at η^{10} than Rh_2O_3/Fe_2O_3.[9,15] However, despite roughly half the Rh content, Rh_2O_3/Fe_2O_3 delivers performance comparable to many noble-metal-based benchmarks, including Rh–Rh_2O_3 and Rh@Pt, in both overpotential and operational stability in acidic conditions.[1,19]

Conclusions

We have established a versatile molecular precursor strategy for the low-temperature preparation of intimately intermixed Rh_2O_3/Fe_2O_3 electrocatalyst, addressing the critical need for scalable, precisely controlled oxide fabrication without high-temperature calcination. By engineering heterobimetallic complex [Rh(acac)$_3$Fe(hfac)$_2$], we enforced exact 1 : 1 Rh : Fe

stoichiometry and achieved uniform atomic-level mixing of Rh^{III} and Fe^{II} ions in heterometallic precursor. Unlike conventional multi-step syntheses, which require high-temperature calcination (400–800 °C) and often yield poorly controlled particle size, collapsed porosity, or impurity products, our molecular precursor approach yields pure Rh_2O_3/Fe_2O_3 nanocomposite at as low as 300 °C. This approach not only halves the Rh loading compared to Rh/Rh_2O_3 standard, but also provides a ligand-directed, low-temperature pathway for designing mixed-oxide electrocatalysts. Given the high cost and scarcity of Rh, our emphasis is on fundamental interfacial chemistry and synthesis, rather than near-term technoeconomic advantages, with Rh_2O_3/Fe_2O_3 serving as a model platform.

Electrochemical evaluation confirms that our Rh_2O_3/Fe_2O_3 composite delivers competitive performance among Rh-containing HER catalysts under acidic conditions, requiring only 32 mV to reach -10 mA cm^{-2} in 0.5 M H_2SO_4, substantially lower than Rh/Rh_2O_3 (140 mV), commercial Rh_2O_3 (260 mV), and α-Fe_2O_3 (210 mV). Tafel and EIS analyses reveal a Volmer–Heyrovsky mechanism with tenfold enhanced interfacial conductivity, while chronopotentiometry demonstrates ultra-stable operation over 120 h with negligible potential drift. Post-stability FESEM confirms preservation of the 3D-sphere morphology, with no evidence of sintering or Ostwald ripening. This robustness likely stems from the intimate intermixing of Rh_2O_3 and Fe_2O_3 oxides. While several Rh-containing and Rh-free systems report lower η[10] under their respective conditions, our results highlight a distinct design principle. This work demonstrates that although the individual sesquioxides (Rh_2O_3 and α-Fe_2O_3) are intrinsically poor HER catalysts, their concerted combination in an intimately intermixed nanocomposite, enabled by our low-temperature molecular-precursor route, delivers markedly enhanced activity and durability, possibly due to intimate mixing, low-temperature synthesis, and interfacial engineering at Rh–Fe–O interfaces. The insights gained in this study regarding ligand-directed metal mixing, structure–property relationships, and degradation suppression should inform future design of mixed-metal oxide electrocatalysts for sustainable hydrogen production.

Author contributions

M. Z. carried out the material synthesis, performed all characterizations and electrochemical experiments, and drafted the initial manuscript; Z. W. conducted single-crystal X-ray data collection and structure refinement, and provided the crystallographic description; M. H. and K. A. D. performed field-emission SEM imaging and energy-dispersive X-ray spectroscopy analyses; E. V. D. conceived the research, supervised the project, and edited the finalized manuscript. All authors have reviewed and approved the final version for publication.

Conflicts of interest

The authors declare no conflict of interest.

Data availability

CCDC 2468531–2468534 contain the supplementary crystallographic data for this paper.[51a–d]

The data supporting this article have been included as part of the SI: experimental procedures, and characterization of all new compounds. See DOI: https://doi.org/10.1039/d5sc04912a.

Acknowledgements

This work was supported by the National Science Foundation grant CHE-2400091 (E. D.). Microscopy facility support provided by the New York State Division of Science, Technology & Innovation's Strategic Initiative "Focus Center New York" at the University of Albany – SUNY (K. D.).

Notes and references

1 M. K. Kundu, R. Mishra, T. Bhowmik and S. Barman, *J. Mater. Chem. A*, 2018, **6**, 23531–23541.
2 R. Arulraj, R. Prabu, C. M. S. Fidha, K. Eswaran, R. Murugesan, S. Shanmugan, A. Maruthapillai and S. Anantharaj, *J. Mater. Chem. A*, 2023, **11**, 25216–25235.
3 H. Zheng, Y. Ding, Q. Wen, S. Zhao, X. He, S. Zhang and C. Dong, *Sci. Total Environ.*, 2022, **802**, 149830.
4 H. Duan, D. Li, Y. Tang, Y. He, S. Ji, R. Wang, H. Lv, P. P. Lopes, A. P. Paulikas, H. Li, S. X. Mao, C. Wang, N. M. Markovic, J. Li, V. R. Stamenkovic and Y. Li, *J. Am. Chem. Soc.*, 2017, **139**, 5494–5502.
5 F. Luo, L. Guo, Y. Xie, J. Xu, W. Cai, K. Qu and Z. Yang, *J. Mater. Chem. A*, 2020, **8**, 12378–12384.
6 M. E. Scofield, Y. Zhou, S. Yue, L. Wang, D. Su, X. Tong, M. B. Vukmirovic, R. R. Adzic and S. S. Wong, *ACS Catal.*, 2016, **6**, 3895–3908.
7 Y. Cheng, S. Lu, F. Liao and M. Shao, *Adv. Funct. Mater.*, 2017, **27**, 1700359.
8 B. Zhang, C. Zhu, Z. Wu, E. Stavitski, Y. H. Lui, T. H. Kim, H. Liu, L. Huang, X. Luan, L. Zhou, K. Jiang, W. Huang, S. Hu, H. Wang and J. S. Francisco, *Nano Lett.*, 2020, **20**, 136–144.
9 X. Li, Y. Huang, Z. Chen, S. Hu, J. Zhu, P. Tsiakaras and P. K. Shen, *Chem. Eng. J.*, 2023, **454**, 140131.
10 H. Jin, M. Ha, M. G. Kim, J. H. Lee and K. S. Kim, *Adv. Energy Mater.*, 2023, **13**, 2204213.
11 S. Zhao, Y. Li and H. Ye, *Chem. Phys. Lett.*, 2024, **834**, 140973.
12 J. N. Tiwari, A. M. Harzandi, M. Ha, S. Sultan, C. W. Myung, H. J. Park, D. Y. Kim, P. Thangavel, A. N. Singh, P. Sharma, S. S. Chandrasekaran, F. Salehnia, J. W. Jang, H. S. Shin, Z. Lee and K. S. Kim, *Adv. Energy Mater.*, 2019, **9**, 1900931.
13 J. N. Tiwari, N. K. Dang, S. Sultan, P. Thangavel, H. Y. Jeong and K. S. Kim, *Nat. Sustain.*, 2020, **3**, 556–563.
14 M. Duan, T. Shu, J. Li, D. Zhang, L.-Y. Gan, K. X. Yao and Q. Yuan, *Nano Res.*, 2023, **16**, 8836–8844.
15 S. Sultan, M. H. Diorizky, M. Ha, J. N. Tiwari, H. Choi, N. K. Dang, P. Thangavel, J. H. Lee, H. Y. Jeong, H. S. Shin, Y. Kwon and K. S. Kim, *J. Mater. Chem. A*, 2021, **9**, 10326–10334.

16 Q. Wang, M. Ming, S. Niu, Y. Zhang, G. Fan and J.-S. Hu, *Adv. Energy Mater.*, 2018, **8**, 1801698.
17 G. Goula, G. Botzolaki, A. Osatiashtiani, C. M. A. Parlett, G. Kyriakou, R. M. Lambert and I. V. Yentekakis, *Catalysts*, 2019, **9**, 541.
18 T. W. Hansen, A. T. Delariva, S. R. Challa and A. K. Datye, *Acc. Chem. Res.*, 2013, **46**, 1720–1730.
19 Y. Zou, R. Goei, S.-A. Ong, A. J. Ong, J. Huang and A. I. Y. Tok, *Processes*, 2022, **10**, 1008.
20 J. Huang, S. N. Guo, L. Sun, X. Zhang, X. Hu and Y. Zhang, *Electrochim. Acta*, 2019, **326**, 134982.
21 *Daily Metal Price: Free Metal Price Tables and Charts*, **https://www.dailymetalprice.com/**, accessed 21 October, 2024.
22 S. S. Narwade, S. M. Mali, V. S. Sapner and B. R. Sathe, *ACS Appl. Nano Mater.*, 2020, **3**, 12288–12296.
23 S. Gnanam and V. Rajendran, *J. Alloys Compd.*, 2013, **550**, 463–470.
24 X. Y. Zhang, H. Yuan, F. Mao, C. F. Wen, L. R. Zheng, P. F. Liu and H. G. Yang, *ChemSusChem*, 2019, **12**, 5063–5069.
25 S. Wei, G. Yang, S. Niu, Z. Ma, J. Jiang, K. Liu, Y. Huang, H. Wang, Y. Cai and Q. Li, *J. Alloys Compd.*, 2024, **976**, 173071.
26 X. Zhang, Y. Guo and C. Wang, *Energy Mater.*, 2024, **4**, 400044.
27 S. Arumugam, Y. Toku and Y. Ju, *Sci. Rep.*, 2020, **10**, 5407.
28 Y. Luo, A. Habrioux, L. Calvillo, G. Granozzi and N. Alonso-Vante, *ChemCatChem*, 2015, **7**, 1573–1582.
29 M. Galceran, M. C. Pujol, J. J. Carvajal, X. Mateos, C. Zaldo, M. Aguil and F. Daz, *J. Lumin.*, 2010, **130**, 1437–1443.
30 S. Hosseini, M. Shaterian, M. Vahedpour and M. A. Rezvani, *Int. J. Hydrogen Energy*, 2018, **43**, 4961–4966.
31 Z. K. Heiba, Y. Akin, W. Sigmund and Y. S. Hascicek, *J. Appl. Crystallogr.*, 2003, **36**, 1411–1416.
32 H. Sun, Z. Yan, C. Tian, C. Li, X. Feng, R. Huang, Y. Lan, J. Chen, C.-P. Li, Z. Zhang and M. Du, *Nat. Commun.*, 2022, **13**, 3857.
33 L. Vayssieres, *Int. J. Nanotechnol.*, 2004, **1**, 1–41.
34 C. M. Lieberman, A. S. Filatov, Z. Wei, A. Y. Rogachev, A. M. Abakumov and E. V. Dikarev, *Chem. Sci.*, 2015, **6**, 2835–2842.
35 Z. Wei, A. S. Filatov and E. V. Dikarev, *J. Am. Chem. Soc.*, 2013, **135**, 12216–12219.
36 C. M. Lieberman, A. S. Filatov, Z. Wei, A. Y. Rogachev, A. M. Abakumov and E. V. Dikarev, *Chem. Sci.*, 2015, **6**, 2835–2842.
37 E. V. Dikarev, H. Zhang and B. Li, *J. Am. Chem. Soc.*, 2005, **127**, 6156–6157.
38 D. S. A. Pratama, A. Haryanto and C. W. Lee, *Front. Chem.*, 2023, **11**, 1141361.
39 G. A. Volpato, D. M. Arboleda, R. Brandiele, F. Carraro, G. B. Sartori, A. Cardelli, D. Badocco, P. Pastore, S. Agnoli, C. Durante, V. Amendola and A. Sartorel, *Nanoscale Adv.*, 2019, **1**, 4296–4300.
40 C. M. Lieberman, M. C. Barry, Z. Wei, A. Y. Rogachev, X. Wang, J. L. Liu, R. Clérac, Y. S. Chen, A. S. Filatov and E. V. Dikarev, *Inorg. Chem.*, 2017, **56**, 9574–9584.
41 J. Gao, W. Yu, J. Liu, L. Qin, H. Cheng, X. Cui and L. Jiang, *J. Colloid Interface Sci.*, 2024, **664**, 766–778.
42 G. Rupprechter, K. Hayek and H. Hofmeister, *J. Catal.*, 1998, **173**, 409–422.
43 J. Hao, S. Peng, H. Li, S. Dang, T. Qin, Y. Wen, J. Huang, F. Ma, D. Gao, F. Li and G. Cao, *J. Mater. Chem. A*, 2018, **6**, 16094–16100.
44 L. Karuppasamy, L. Gurusamy, S. Anandan, S. C. Barton, C. H. Liu and J. J. Wu, *Chem. Eng. J.*, 2024, **495**, 153442.
45 Z. Xie, Z. Xie, W. Wang, D. Ding, Y. Zou, Y. Zou, Y. Cui, L. Xu, J. Jiang and J. Jiang, *J. Mater. Chem. A*, 2020, **8**, 12169–12176.
46 H. Borg, I. Morales, D. Kranz, N. C. Bigall and D. Dorfs, *Catalysts*, 2023, **13**, 1074.
47 U. Martinez, A. Serov, M. Padilla, P. Atanassov, presented in part at, *224th Electrochemical Society Meeting*, San Francisco, CA, USA, October, 2013.
48 H. L. Guo, X. F. Wang, Q. Y. Qian, F. B. Wang and X. H. Xia, *ACS Nano*, 2009, **3**, 2653–2659.
49 Y. Zhu, K. Fan, C.-S. Hsu, G. Chen, C. Chen, T. Liu, Z. Lin, S. She, L. Li, H. Zhou, Y. Zhu, H. M. Chen and H. Huang, *Adv. Mater.*, 2023, **35**, 2301133.
50 A. Pei, R. Xie, Y. Zhang, Y. Feng, W. Wang, S. Zhang, Z. Huang, L. Zhu, G. Chai, Z. Yang, Q. Gao, H. Ye, C. Shang, B. H. Chen and Z. Guo, *Energy Environ. Sci.*, 2023, **16**, 1035–1048.
51 (*a*) M. Zulqarnain, Z. Wei, M. Hollo, K. A. Dunn and E. V. Dikarev, CCDC 2468531: Experimental Crystal Structure Determination, 2025, DOI: **10.5517/ccdc.csd.cc2nvq19**; (*b*) M. Zulqarnain, Z. Wei, M. Hollo, K. A. Dunn and E. V. Dikarev, CCDC 2468532: Experimental Crystal Structure Determination, 2025, DOI: **10.5517/ccdc.csd.cc2nvq2b**; (*c*) M. Zulqarnain, Z. Wei, M. Hollo, K. A. Dunn and E. V. Dikarev, CCDC 2468533: Experimental Crystal Structure Determination, 2025, DOI: **10.5517/ccdc.csd.cc2nvq3c**; (*d*) M. Zulqarnain, Z. Wei, M. Hollo, K. A. Dunn and E. V. Dikarev, CCDC 2468534: Experimental Crystal Structure Determination, 2025, DOI: **10.5517/ccdc.csd.cc2nvq4d**.